Bergische Universität Wuppertal

Fakultät für Mathematik und Naturwissenschaften

Institute of Mathematical Modelling, Analysis and Computational Mathematics (IMACM)

Preprint BUW-IMACM 24/05

Sergey Pereselkov, Venedikt Kuz'kin, Matthias Ehrhardt,
Yurii Matvienko, Sergey Tkachenko, and Pavel Rybyanets

Formation of 2D-Holograms of Noise Source and Bearing Estimation by a Vector Scalar Receiver in the High-Frequency Band

March 11, 2024

http://www.imacm.uni-wuppertal.de

Journal of
Marine Science and Engineering

MDPI

Article

Formation of 2D-Holograms of Noise Source and Bearing Estimation by a Vector Scalar Receiver in the High-Frequency Band

Sergey Pereselkov [1,*], Venedikt Kuz'kin [2], Matthias Ehrhardt [3], Yurii Matvienko [4], Sergey Tkachenko [1] and Pavel Rybyanets [1]

[1] Voronezh State University, Mathematical Physics and Information Technology Department, 394018 Voronezh, Russia; tkachenko.edu@yandex.ru (S.T.); rybyanets.edu@yandex.ru (P.R.)
[2] Prokhorov General Physics Institute of the Russian Academy of Sciences, 119991, Moscow, Russia ; kumiov@yandex.ru
[3] University of Wuppertal, Chair of Applied and Computational Mathematics, Gaußstraße 20, 42119 Wuppertal, Germany; ehrhardt@uni-wuppertal.de
[4] Institute of Marine Technology Problems, Far East Branch, Russian Academy of Sciences, 690091, Vladivostok, Russia; ymat33@yandex.ru
* Correspondence: pereselkov@yandex.ru

Abstract: The method of formation of the 2D-interferogram and 2D-hologram of a noise source by a vector scalar receiver in the high-frequency band in a shallow water waveguide is presented in the paper. The interferograms and holograms for different channels of the vector scalar receiver are considered. It is shown that 2D-interferogram consists of parallel interference fingers in presence of moving noise source. As a result, the hologram contains focal points located on a straight line. At presence of moving source the angular distribution of holograms has the main extreme value. Thus, it is possible to detect and locate the noise source in the shallow water waveguide within the framework of holographic signal processing. The moving direction of the noise source can be estimated by the slope of the interference fringes and the angular coefficient of the straight line of the focal points in the hologram domain. The results of noise filtering within the framework of holographic signal processing are demonstrated in the paper. It is shown in the paper that within the framework of holographic signal processing the temporal dependence of the source bearing is estimated by using the relation between the main extreme values of angular distributions of holograms for X-channel and Y-channel of vector scalar receiver. The results of reconstruction of the source bearing within the framework of numerical simulation and experimental data processing. The bearing source values reconstructed within holographic signals processing are close to the values defined by the geometry of the source trajectory.

Keywords: shallow water; noise source; sound field; sound rays; interference; interferogram; hologram; source detection; source bearing

Citation: Pereselkov, S.; Kuz'kin, V.; Ehrhardt, M.; Tkachenko, S.; Rybyanets, P. Formation of 2D-Holograms of Noise Source and Bearing Estimation by a Vector Scalar Receiver in the High-Frequency Band. *J. Mar. Sci. Eng.* **2023**, *1*, 0. https://doi.org/

Academic Editor: Rouseff Daniel

Received: 13 January 2023
Revised: 26 February 2023
Accepted: 1 March 2023
Published:

1. Introduction

The problem of source detection and localization in shallow water has attracted considerable interest in underwater acoustics. One of the ways to solve this problem is *Matched Field Processing* (MFP) [1–4]. Within the MFP method, the signal replica is simulated for the shallow water waveguide model, and then the source coordinates of the signal replica closest to the experimental signal are selected as the source location. However, the main problem of MFP is the need to use waveguide model with parameters close to experimental waveguide. Often, it is impossible to create such a waveguide model due to the spatio-temporal variability of the oceanic environment. Therefore, there is a need to develop alternative methods for source detection and localization in shallow water waveguide.

Recently, there has been a great scientific interest in interferometric signal processing in underwater acoustics. The *interferometric signal processing* (ISP) is based on stable features of the interference structure (pattern) of the broadband sound field in the shallow water waveguide [5,6]. The sound field normal mode interference in underwater waveguides results in specific patterns within the sound intensity distribution, observable both in the frequency domain, as noted by Chuprov [5], and in the frequency-time domain, as outlined by Weston and Stevens [6]. The seminal work of Chuprov [5] laid the foundation for the mathematical theory of sound field interference in underwater acoustics. Chuprov introduces the concept of the waveguide invariant – a key factor in the analysis of interference patterns within the sound field. Such interference in underwater waveguides produces observable, organized patterns in sound intensity seen in the frequency-time domain (see Weston and Stevens [6]) and the frequency-range domain (Chuprov [5]). The basic principles of sound interference in underwater acoustics were established by Chuprov [5], who also introduced the concept of waveguide invariance, which marks a critical aspect of the interference pattern of the sound field. Notable advances in the theory of interference are detailed in subsequent research by Grachev [7], Orlov and Sharonov [8], Ianniello [9], and in the conference proceedings edited by Kuperman and D'Spain [10].

D'Spain and Kuperman [11] used the waveguide invariant for single hydrophone spectrograms in shallow water environments. Heaney and Cox [12] proposed an incoherent method for geoacoustic characterization. Thode [13] used a vertical receiving array and a guide source to construct a virtual receiver. Hodgkiss et al. [14] used the concept to move the focal plane in a time-reversal experiment. Thode et al. [15] studied the sidelobe structure of a matched-field processor. Yang [16] used waveguide invariant theory for source motion compensation. Yang [17], Rouseff and Leigh [18] Striation patterns can also be observed in the output of a coherent processor such as a horizontal line array beamformer. In the paper Thode [19] develops the waveguide-invariant theory for source ranging with minimal environmental information. In the papers Rouseff and Leigh [20], Baggeroe [21], ISP is developed for estimating invariant parameters of waveguides. In the work of Heaney [22], ISP is used to classify the seabed based on passing ship signals. In the work of Cockrell and Schmidt [23], the ISP is offered to estimate the source range in shallow water. The ISP is used in Rouseff and Zurk [24] for range-independent invariant estimation. The ISP approach is used in Harrison [25] to explain interference fringes by the arrival times of the eigenrays. The ISP is developed in the papers of Bonnel et al. [26,27] for deep-sea passive sonar. Wang and Gao [28–30] have applied dispersion elimination technology to shallow water acoustic signal processing and made some research achievements. Guo [31] proposed a method to estimate the range and depth by using a single hydrophone based on the relationship of the horizontal wavenumber difference between two modes, with the waveguide invariant, for low-frequency underwater acoustic pulse signals in a range-independent shallow-water waveguide. Zhang [32] proposed a method using the de-dispersive transform to extract the source position information from the dispersion. The result of numerical simulation shows that the method is effective. Lee and Makris [33–35] proposed the concept of array invariant. This approach provides reasonable source range estimation with little computational effort, full array gain, and minimal knowledge of the environment.

One of the most advantageous approaches of ISP is *holographic signal processing* (HSP) [36–42]. The physical and mathematical principles of hologram formation were first described by Kuz'kin and Pereselkov [36]. In papers [37] and [38] the HSP is analyzed for low-frequency band in regular waveguide. In paper [39] the resolution of sources by HSP is offered. In paper [40] the HSP is developed for noise source. In papers [41] and [41] and the HSP is developed for irregular waveguide at presence of internal waves.

In the development of HSP it was assumed that acoustic signals of the source are recorded by hydrophone (sound pressure) in low-frequency band. However, in many useful cases acoustic signals are recorded by *vector scalar receiver* (VSR) [42–47] in high-frequency band ($0 - 10$ kHz). VSR and high-frequency band give us additional capabilities.

VSR allows to record the acoustic signals on fourth channels: sound pressure $P(t)$, $V_X(t)$, $V_Y(t)$, $V_Z(t)$ components of vibration velocities [42–45]. Thus, it is important to consider the HSP when using VSR in the high-frequency band.

The aim of this paper is to present the results of theoretical analysis, numerical modeling and experimental verification of holographic signal processing for noise source by VSR in high-frequency band ($0 - 10$ kHz). The method of formation of 2D interferogram and 2D hologram of a noise source by vector scalar receiver in high-frequency band in a shallow water waveguide is developed in the paper. The interferograms and holograms for different channels of the vector scalar receiver are considered. It is shown that 2D interferogram consists of parallel interference fingers in presence of moving noise source. As a result, the hologram contains focal points located on a straight line. At presence of moving source the angular distribution of holograms has the main extreme value. Thus, it is possible to detect and locate the noise source in the shallow water waveguide within the framework of holographic signal processing. It is shown in the paper that within the framework of holographic signal processing the temporal dependence of the source bearing is estimated by using the relation between main extreme values of angular distributions of holograms for X-channel and Y-channel of vector scalar receiver. The results of reconstruction of the source bearing within the framework of numerical simulation and experimental data processing. The bearing source values reconstructed within holographic signals processing are close to the values defined by the geometry of the source trajectory.

The paper consists of five sections. The review of papers related to signal processing based on waveguide invariant in shallow water is presented in Section 1. The theory of holographic signal processing by VSR in the high-frequency band in shallow-water waveguide is described in Section 2. The results of holographic signal processing obtained by numerical modeling are considered in Section 3. The results of holographic signal processing in the context of experimental data processing are analyzed in Section 4. In the conclusion, Section 5, the presented results are summarized.

2. Holographic Method of the Signal Processing in a Shallow Water Waveguide

2.1. High-Frequency Sound Field of a Moving Source in Shallow Water

Consider the high-frequency sound field in a 3D model of a shallow water waveguide. The vertical plane of the waveguide is shown in Figure 1. The horizontal plane of the waveguide is shown in Figure 2. The waveguide in the coordinate system (X, Y, Z) is represented as a layer of water with sound speed $c(\vec{r}, z)$. Here $\vec{r} = (x, y)$ is the radius vector in the horizontal plane. The water layer is limited at depth by a free surface $(z = 0)$ and the sea bottom $(z = H)$. The reflection coefficient of the water-bottom boundary is W.

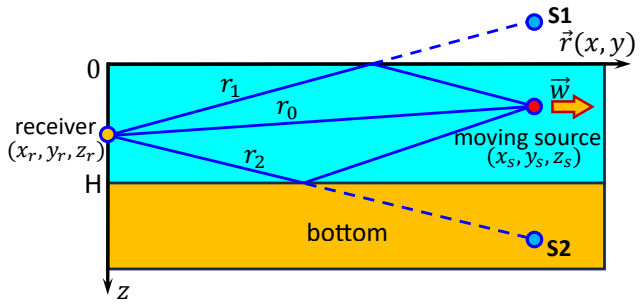

Figure 1. Shallow Water Waveguide Geometry. Vertical plane $(\vec{r}, z)$.

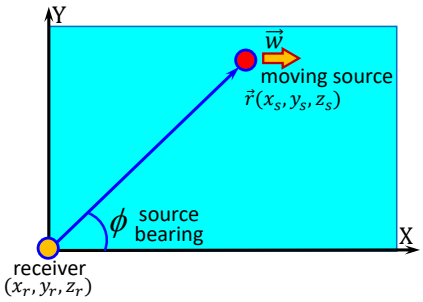

Figure 2. Shallow Water Waveguide Geometry. Horizontal plane (x, y).

The receiver is located at point $Q(x_r, y_r, z_r)$. The high-frequency sound source is moving at point $S(x_s(t), y_s(t), z_s(t))$. The velocity of the source is denoted by $\vec{w}$. The spectrum of the signal emitted by the source is $s(\omega)$, with $\omega = 2\pi f$.

The complex sound pressure can be written as [48,49],

$$P(\vec{r}(t), z_s, z_r, \omega) = s(\omega) \sum_{m=0}^{\infty} (-W)^m \left[\frac{\exp\left(ik(\omega) r_{m0}\right)}{r_{m0}} - \frac{\exp\left(ik(\omega) r_{m1}\right)}{r_{m1}} + \right.$$
$$\left. + W \frac{\exp\left(ik(\omega) r_{m2}\right)}{r_{m2}} - W \frac{\exp\left(ik(\omega) r_{m3}\right)}{r_{m3}} \right], \quad (1)$$

where $\vec{r}(t) = |\vec{r}_r - \vec{r}_s(t)|$ denotes the distance between source and receiver. $k(\omega) = \omega/c$ denotes the sound wavenumber. Here, in (1) we used the notation

$$r_{mj} = \left(r^2 + z_{mj}^2\right)^{1/2}, \quad (2)$$

where the values z_{mj} are defined as follows

$$\begin{aligned} z_{m0} &= 2Hm + z_s - z_r; \quad z_{m1} = 2H(m+1) - z_s - z_r; \\ z_{m2} &= 2Hm + z_s + z_r; \quad z_{m3} = 2H(m+1) - z_s + z_r; \\ & \qquad m = 0, 1, 2, \ldots; \quad j = 0, 1, 2, 3. \end{aligned} \quad (3)$$

The vibration acceleration (particle acceleration) complex field $\mathbf{A} = (A_X, A_Y, A_Z)$ is expressed by the sound pressure Eq. (1) in the following way [43]:

$$\mathbf{A} = -\frac{1}{\rho} \nabla P. \quad (4)$$

Using the ray decomposition of the sound pressure field, expressions for the horizontal acceleration components can be obtained:

$$\begin{aligned} A_X\left(\vec{r}(t), z_s, z_r, \omega\right) &= -\frac{1}{\rho} \frac{\partial P}{\partial x} \\ &= -s(\omega) \frac{r}{\rho} \sum_{m=0}^{\infty} (-W)^m \left[\frac{\exp\left(ik(\omega) r_{m0}\right)\left(ikr_{m0} - 1\right)}{r_{m0}^3} - \frac{\exp\left(ik(\omega) r_{m1}\right)\left(ikr_{m1} - 1\right)}{r_{m1}^3} \right. \\ &\quad \left. + W \frac{\exp\left(ik(\omega) r_{m2}\right)\left(ikr_{m2} - 1\right)}{r_{m2}^3} - W \frac{\exp\left(ik(\omega) r_{m3}\right)\left(ikr_{m3} - 1\right)}{r_{m3}^3} \right] \frac{\partial r}{\partial x}, \end{aligned} \quad (5)$$

$$
\begin{aligned}
&A_Y\left(\vec{r}(t), z_s, z_r, \omega\right) = -\frac{1}{\rho}\frac{\partial P}{\partial y} \\
&= -s(\omega)\frac{r}{\rho}\sum_{m=0}^{\infty}(-W)^m\left[\frac{\exp\left(\mathrm{i}k(\omega)r_{m0}\right)\left(\mathrm{i}kr_{m0}-1\right)}{r_{m0}^3} - \frac{\exp\left(\mathrm{i}k(\omega)r_{m1}\right)\left(\mathrm{i}kr_{m1}-1\right)}{r_{m1}^3}\right. \\
&\quad \left. + W\frac{\exp\left(\mathrm{i}k(\omega)r_{m2}\right)\left(\mathrm{i}kr_{m2}-1\right)}{r_{m2}^3} - W\frac{\exp\left(\mathrm{i}k(\omega)r_{m3}\right)\left(\mathrm{i}kr_{m3}-1\right)}{r_{m3}^3}\right]\frac{\partial r}{\partial y}.
\end{aligned} \tag{6}
$$

The vibration velocity (particle velocity) complex field $\mathbf{V} = (V_X, V_Y, V_Z)$ is expressed by the vibration acceleration Eq. (4):

$$
\mathbf{V} = \frac{\mathrm{i}}{\omega}\mathbf{A} = -\frac{\mathrm{i}}{\omega\rho}\nabla P. \tag{7}
$$

The final formulas for horizontal components of vibration velocity complex field are:

$$
\begin{aligned}
&V_X\left(\vec{r}(t), z_s, z_r, \omega\right) = \frac{\mathrm{i}}{\omega}A_X \\
&= -s(\omega)\frac{\mathrm{i}r}{\omega\rho}\sum_{m=0}^{\infty}(-W)^m\left[\frac{\exp\left(\mathrm{i}k(\omega)r_{m0}\right)\left(\mathrm{i}kr_{m0}-1\right)}{r_{m0}^3} - \frac{\exp\left(\mathrm{i}k(\omega)r_{m1}\right)\left(\mathrm{i}kr_{m1}-1\right)}{r_{m1}^3}\right. \\
&\quad \left. + W\frac{\exp\left(\mathrm{i}k(\omega)r_{m2}\right)\left(\mathrm{i}kr_{m2}-1\right)}{r_{m2}^3} - W\frac{\exp\left(\mathrm{i}k(\omega)r_{m3}\right)\left(\mathrm{i}kr_{m3}-1\right)}{r_{m3}^3}\right]\frac{\partial r}{\partial x},
\end{aligned} \tag{8}
$$

$$
\begin{aligned}
&V_Y(\vec{r}(t), z_s, z_r, \omega) = \frac{\mathrm{i}}{\omega}A_Y = \\
&= -s(\omega)\frac{\mathrm{i}r}{\omega\rho}\sum_{m=0}^{\infty}(-W)^m\left[\frac{\exp\left(\mathrm{i}k(\omega)r_{m0}\right)\left(\mathrm{i}kr_{m0}-1\right)}{r_{m0}^3} - \frac{\exp\left(\mathrm{i}k(\omega)r_{m1}\right)\left(\mathrm{i}kr_{m1}-1\right)}{r_{m1}^3}\right. \\
&\quad \left. + W\frac{\exp\left(\mathrm{i}k(\omega)r_{m2}\right)\left(\mathrm{i}kr_{m2}-1\right)}{r_{m2}^3} - W\frac{\exp\left(\mathrm{i}k(\omega)r_{m3}\right)\left(\mathrm{i}kr_{m3}-1\right)}{r_{m3}^3}\right]\frac{\partial r}{\partial y}.
\end{aligned} \tag{9}
$$

Taking into account $\partial r/\partial x = \cos\phi$, $\partial r/\partial y = \sin\phi$, we can simplify the Eq. (8) and Eq. (9):

$$
V_X = V_R\cos\phi, \quad V_Y = V_R\sin\phi, \tag{10}
$$

where ϕ is source bearing, V_R is vibration velocity complex field in horizontal plane:

$$
\begin{aligned}
&V_R\left(\vec{r}(t), z_s, z_r, \omega\right) \\
&= -s(\omega)\frac{\mathrm{i}r}{\omega\rho}\sum_{m=0}^{\infty}(-W)^m\left[\frac{\exp\left(\mathrm{i}k(\omega)r_{m0}\right)\left(\mathrm{i}kr_{m0}-1\right)}{r_{m0}^3} - \frac{\exp\left(\mathrm{i}k(\omega)r_{m1}\right)\left(\mathrm{i}kr_{m1}-1\right)}{r_{m1}^3}\right. \\
&\quad \left. + W\frac{\exp\left(\mathrm{i}k(\omega)r_{m2}\right)\left(\mathrm{i}kr_{m2}-1\right)}{r_{m2}^3} - W\frac{\exp\left(\mathrm{i}k(\omega)r_{m3}\right)\left(\mathrm{i}kr_{m3}-1\right)}{r_{m3}^3}\right].
\end{aligned} \tag{11}
$$

In the rest of the text, the following notation is used for the sound pressure: $P(f,t)$, and the vibration velocity components: $V_X(f,t)$, $V_Y(f,t)$, $V_R(f,t)$:

$$
\begin{aligned}
P(f,t) &= P(\vec{r}(t), z_s, z_r, \omega), \\
V_X(f,t) &= V_X(\vec{r}(t), z_s, z_r, \omega), \\
V_Y(f,t) &= V_Y(\vec{r}(t), z_s, z_r, \omega), \\
V_R(f,t) &= V_R(\vec{r}(t), z_s, z_r, \omega).
\end{aligned} \tag{12}
$$

2.2. 2D-Interferograms of the Moving Source Formed by a Vector Scalar Receiver

In frequency-time variables (f,t) we introduce the notation for interferograms:

$$\begin{aligned} I_P(f,t) &= P(f,t)P^*(f,t), \\ I_X(f,t) &= V_X(f,t)V_r^*(f,t), \\ I_Y(f,t) &= V_Y(f,t)V_r^*(f,t), \\ I_R(f,t) &= V_R(f,t)V_r^*(f,t). \end{aligned} \tag{13}$$

The superscript asterisk means complex conjugation. Here $I_P(f,t)$ is the interferogram of the sound pressure. $I_X(f,t)$, $I_Y(f,t)$, $I_R(f,t)$ are the interferograms of the horizontal components of the vibration velocities. The interferogram of the sound pressure $I_P(f,t)$ is analyzed in detail in the papers [37,38]. The interferograms of the horizontal components of the vibration velocities $I_X(f,t)$, $I_Y(f,t)$, $I_R(f,t)$ have the same structure and characteristics. Thus, the method of description of the sound pressure interferogram described in [37,38] is applicable to analysis of vibration velocity interferograms.

2.3. 2D-Holograms of the Moving Source Formed by a Vector Scalar Receiver

In holographic signal processing, the quasi-coherent accumulation of the intensity distributions: $I_P(f,t)$, $I_X(f,t)$, $I_Y(f,t)$, $I_R(f,t)$ in frequency-time coordinates [37,38]. The 2D Fourier transform (2D-FT) is applied to the accumulated intensity of the interferograms $I(f,t)$. The 2D-FT of the interferogram $I(\omega,t)$ is called *Fourier hologram* (hologram) $F(\tau,\nu)$. The hologram $F(\tau,\nu)$ allows to concentrate the intensity of the interferograms $I(f,t)$ due to the interference fingers in focal points.

Consider 2D holograms of sound pressure and horizontal components of vibration velocities:

$$\begin{aligned} F_P(\tau,\nu) &= \int_0^{\Delta t}\int_{f_1}^{f_2} I_P(f,t)\exp\left[\mathrm{i}2\pi(\nu t - f\tau)\right] dtdf, \\ F_X(\tau,\nu) &= \int_0^{\Delta t}\int_{f_1}^{f_2} I_X(f,t)\exp\left[\mathrm{i}2\pi(\nu t - f\tau)\right] dtdf, \\ F_Y(\tau,\nu) &= \int_0^{\Delta t}\int_{f_1}^{f_2} I_Y(f,t)\exp\left[\mathrm{i}2\pi(\nu t - f\tau)\right] dtdf, \\ F_R(\tau,\nu) &= \int_0^{\Delta t}\int_{f_1}^{f_2} I_R(f,t)\exp\left[\mathrm{i}2\pi(\nu t - f\tau)\right] dtdf. \end{aligned} \tag{14}$$

Here ν and τ - frequency and time of the hologram domain; Δt - observation time; $f_{1,2} = f_0 \mp (\Delta f/2)$, f_0 and Δf - average frequency and spectrum width; the initial time $t = 0$. The expression under the modulus sign describes the trajectory accumulation J of independent complex signal amplitudes in the frequency band Δf during the observation time Δt. The number of samples J is determined:

$$J = \frac{\Delta t}{\delta t_1 + \delta t_2}, \tag{15}$$

where δt_1 and δt_2 are the duration of the signal realizations and the time interval between them. Realizations are independent if $\delta t_2 > 2\pi/\Delta\omega$.

The spectral density of the hologram $F(\tau,\nu)$ is localized in focal points, mirrored with respect to the origin [37,38]. They are located in the first and third quadrants when the source moves to the receiver $(w < 0)$. They are in the second and fourth quadrants as the source moves away from the receiver $(w > 0)$. Focal points located in the first and fourth quadrants are the real image of the source, and in the second and third quadrants - a virtual

image. The spectral density of the hologram $F(\tau, \nu)$ is mainly concentrated in the band bounded by straight lines [37,38]:

$$\nu = \tilde{\varepsilon}\tau + \delta\nu, \qquad \nu = \tilde{\varepsilon}\tau - \delta\nu, \tag{16}$$

where $\delta\nu = 1/\Delta t$ is the half-width of the focal points in the direction of the axis ν, $\tilde{\varepsilon}$ is the angular coefficient of the line on which the coordinates of the focal points are located. In the direction of the axis, the half-width of the focal spots is $\delta\tau = 1/\Delta f$. Outside this band the spectral density of the hologram is practically suppressed. The angular coefficients of the interference fringes $\delta f/\delta t$ are defined by the expression

$$\tilde{\varepsilon} = -\frac{\delta f}{\delta t}, \tag{17}$$

where δf - frequency shift of the wave field maximum over time δt.

2.4. Detection of the Moving Source

Consider the angular distribution of the spectral density of the holograms $F_P(f,t)$, $F_X(f,t)$, $F_Y(f,t)$, $F_R(f,t)$:

$$\begin{aligned} G_P(\chi) &= \int_0^{\Delta\tau} \left|F_P(\tau, \chi\tau)\right| d\tau, \\ G_X(\chi) &= \int_0^{\Delta\tau} \left|F_X(\tau, \chi\tau)\right| d\tau, \\ G_Y(\chi) &= \int_0^{\Delta\tau} \left|F_Y(\tau, \chi\tau)\right| d\tau, \\ G_R(\chi) &= \int_0^{\Delta\tau} \left|F_R(\tau, \chi\tau)\right| d\tau, \end{aligned} \tag{18}$$

The function $G(\chi)$ has maximum value at $\chi = \chi_{\max}$ if the source is present. The direction of the maximum value is defined by ε. The maximum value of $G(\chi_{\max})$ is two or more times higher than the values in the other directions ($\chi \neq \chi_{\max}$):

$$G(\chi_{\max}) \geq 2G(\chi). \tag{19}$$

The Eq. (19) is the criterion for source detection.

- If this condition is met, the source is present in the waveguide;
- if the condition is not satisfied, the source is absence.

Here $\Delta\tau$ is the linear size of the focal point along the τ-axis; χ is the angular coefficient of the straight lines $\nu = \chi\tau$ in the hologram domain. Information about the transfer function of the medium is not required. If the criterion Eq. (19) is fulfilled, the estimates of the moving source parameters (bearing, radial velocity, range, depth) in holographic signal processing are close to the true values [37,38].

2.5. Source Bearing Estimation

Let us consider the method of source bearing estimation. The holograms F_X, F_Y up to the factors $\cos\phi$ and $\sin\phi$ reproduce the hologram F_R, where ϕ is the source bearing (Figure 2) - the angle in the horizontal plane between the axis X of the VSR and the direction to the source. Therefore

$$\tan\phi = \frac{G_Y(\chi_{\max})}{G_X(\chi_{\max})}. \tag{20}$$

The determination of the direction to the source is ambiguous: the bearings $\pm\phi$, $\pi \pm \phi$ are indistinguishable. The inverse 2D Fourier transform is used to recover the interferograms

I_X, I_Y, I_R. The ambiguity of the bearing is removed by determining the sign of the ratio of the interferograms

$$\frac{I_X(f,t)}{I_R(f,t)} = \gamma_X, \qquad \frac{I_Y(f,t)}{I_R(f,t)} = \gamma_Y. \tag{21}$$

The criterion for unambiguous source bearing estimation:

- if $\gamma_X > 0$, $\gamma_Y > 0$, then the source is located in the I-th quadrant of the VSR;
- if $\gamma_X < 0$, $\gamma_Y > 0$, then the source is located in the II-th quadrant of the VSR;
- if $\gamma_X < 0$, $\gamma_Y < 0$, then the source is located in the III-th quadrant of the VSR;
- if $\gamma_X > 0$, $\gamma_Y < 0$, then the source is located in the IV-th quadrant of the VSR.

3. Numerical Simulation Results

Let us consider the following model of the shallow water waveguide, which is close to the experimental waveguide. The vertical plane of the waveguide is shown in Figure 3. The depth of the waveguide is $H = 15$ m. The sound velocity profile of the water layer is constant $c_w(z) = 1400$ m/s. The parameters of the liquid absorbing bottom: sound velocity $c_b = 1780$ m/s, density $\rho_b = 2.0$ g/cm^3. The sound source at a depth of $z_s = 5$ m moves along the trajectory shown in Figure 4. The source speed is $v = 1.5$ m/s. The high-frequency band is $\Delta f = 9$ kHz (2.5 − 11.5 kHz). The receiver is located at a point at a depth of $z_q = 15$ m.

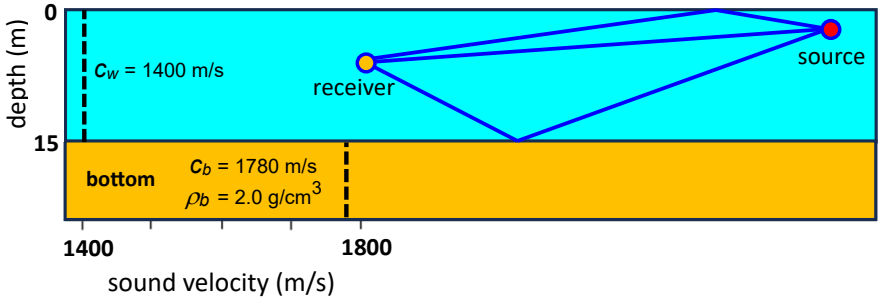

Figure 3. Model Parameters for the Shallow Water Waveguide.

The trajectory of the noise source in the horizontal plane of the waveguide is shown in Figure 4. The source moves along a straight line (A→B→C) which is parallel to the x-axis.

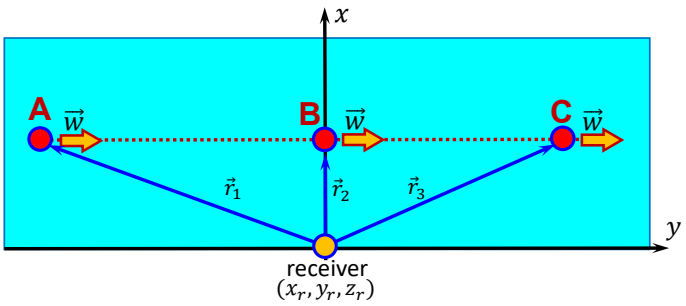

Figure 4. Trajectory of the noise source. Horizontal plane. A - Starting point. B - Traverse point. C - Finish point.

The source trajectory parameters.

- receiver is located in point: ($x_r = 0$ m, $y_r = 0$ m, $z_r = 15$ m);
- source velocity: $w = 1.5$ m/s;
- motion time: $\Delta t = 0 - 15$ min;
- motion starting point: A ($x_s = 150$ m, $y_s = -675$ m, $z_s = 5$ m), $r_1 = 700$ m;
- motion traverse point: B ($x_s = 150$ m, $y_s = 0$ m, $z_r = 5$ m), $r_2 = 150$ m;
- motion finish point: C ($x_s = 150$ m, $y_s = 675$ m, $z_r = 5$ m), $r_3 = 700$ m.

The time dependence of coordinate $y_s(t)$ is:

$$y_s(t) = -675 + 1.5\,t.$$

The time dependence of range $r_s(t)$ between source and receiver is:

$$r_s(t) = \sqrt{(150)^2 + (-675 + 1.5\,t)^2}.$$

The results of numerical modeling are shown in Figures 5–10. The interferogram of the sound pressure $I_P(f,t)$ for the time of motion $\Delta t = 0 - 15$ min, in the frequency band $\Delta f = 2.5 - 11.5$ kHz is shown in Figure 5. The interferogram $I_P(f,t)$, hologram $F_P(\tau,\nu)$ and angular distribution $G_P(\chi)$ for different cases of source motion are shown in Figures 6–9.

Let us consider the results of numerical modeling of the interferogram $I_P(f,t)$ for a source moving along the trajectory A→B→C (Figure 5) in the time-frequency domain. It can be seen that the interferogram of the sound pressure $I_P(f,t)$ has a quasi-periodic structure (T_f - period in the frequency domain). If the source moves from point A to point B, the interferogram period decreases from $T_f = 9$ kHz to $T_f = 1.8$ kHz. The slope of the interference fringes is negative: $\delta f/\delta t = -1.5$ kHz/min. When the source passes through the traverse zone, the interferogram period is $T_f = 1.8$ kHz. The interference fringes are parallel to the t axis. As a result, $\delta f/\delta t = 0$ kHz/min. As the source moves from point B to point C, the interferogram period increases from $T_f = 1.8$ kHz to $T_f = 9$ kHz. The slope of the interference fringes is positive: $\delta f/\delta t = +1.5$ kHz/min.

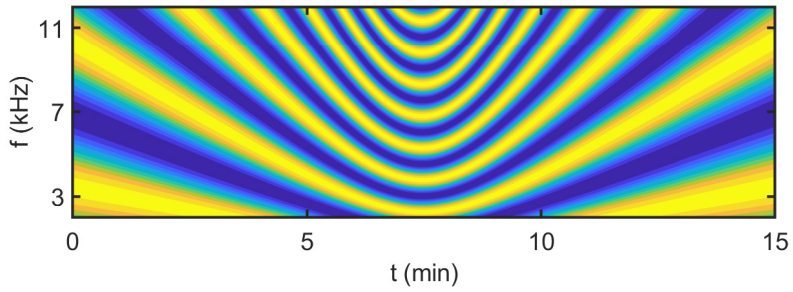

Figure 5. Interferogram $I_P(f,t)$ of a source moving along the trajectory A→B→C in the frequency band $\Delta f = 2.5 - 11.5$ kHz.

The interferogram $I_P(f,t)$, hologram $F_P(\tau,\nu)$ and angular distribution $G_P(\chi)$ for three cases of source motion are shown in Figures 6–9.

The $I_P(f,t)$, $F_P(\tau,\nu)$ and $G_P(\chi)$ for the case of the source moving from point A to point B in the time interval $\Delta t = 2.5 - 4.2$ min are shown in Figure 6. It can be seen that the slope of the interference fringes is negative: $\delta f/\delta t = -1.5$ kHz/min on the interferogram (Figure 6 (a)). As a result, the focal points lie on a straight line $\nu = \tilde{\varepsilon}\tau$ with an angular coefficient $\tilde{\varepsilon} = 40$ Hz/s in the hologram $F_P(\tau,\nu)$ domain (Figure 6 (b)). The angular distribution $G_P(\chi)$ has an extreme value at point $\chi \approx -0.025\ s^{-2}$ (Figure 6 (c)).

The $I_P(f,t)$, $F_P(\tau,\nu)$ and $G_P(\chi)$ for the case of the source moving at point B (traverse) in the time interval $\Delta t = 6.7 - 8.4$ min are shown in Figure 7. It can be seen that the slope of the interference fringes is approximately zero. $\delta f/\delta t = 0$ kHz/min on the interferogram (Figure 7 (a)). As a result, the focal points are located at points on a straight line $\nu = \tilde{\varepsilon}\tau$ with an angular coefficient of $\tilde{\varepsilon} = 0$ Hz/s in the hologram $F_P(\tau,\nu)$ domain (Figure 7 (b)). The angular distribution $G_P(\chi)$ has an extreme value at the point $\chi \approx 0\ s^{-2}$ (Figure 7 (c)).

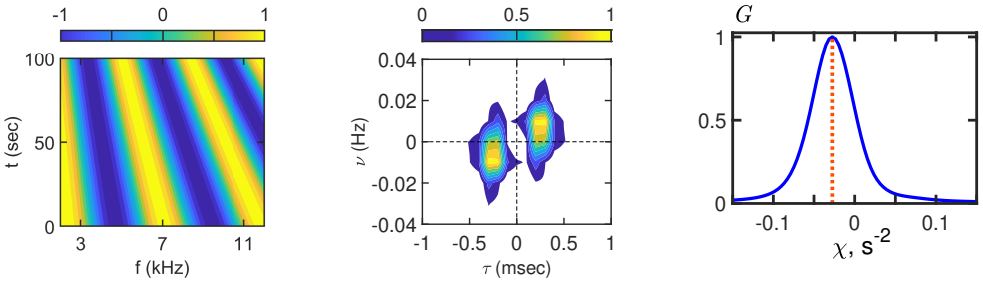

(a) (b) (c)

Figure 6. Interferogram $I_P(f,t)$ (a), hologram $F_P(\tau,\nu)$ (b), angular distribution $G_P(\chi)$ (c). Time: $\Delta t = 2.5 - 4.2$ min. Frequency: $\Delta f = 2.5 - 11.5$ kHz.

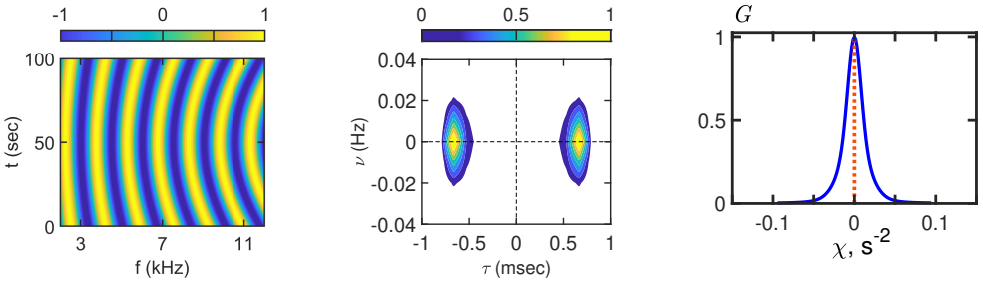

(a) (b) (c)

Figure 7. Interferogram $I_P(f,t)$ (a), hologram $F_P(\tau,\nu)$ (b), angular distribution $G_P(\chi)$ (c). Time: $\Delta t = 6.7 - 8.4$ min. Frequency: $\Delta f = 2.5 - 11.5$ kHz.

The $I_P(f,t)$, $F_P(\tau,\nu)$ and $G_P(\chi)$ for the case of the source moving from point B to point C in the time interval $\Delta t = 10.8 - 12.5$ min are shown in Figure 8. It can be seen that the slope of the interference fringes is negative. $\delta f/\delta t = +1.5$ kHz/min on the interferogram (Figure 8 (a)). As a result, the focal points are on points on a straight line $\nu = \tilde{\varepsilon}\tau$ with an angular coefficient of $\tilde{\varepsilon} = -40$ Hz/s in the domain of the hologram $F_P(\tau,\nu)$ (Figure 8 (b)). The angular distribution $G_P(\chi)$ has an extreme value at the point $\chi \approx= +0.025\ s^{-2}$ (Figure 8 (c)).

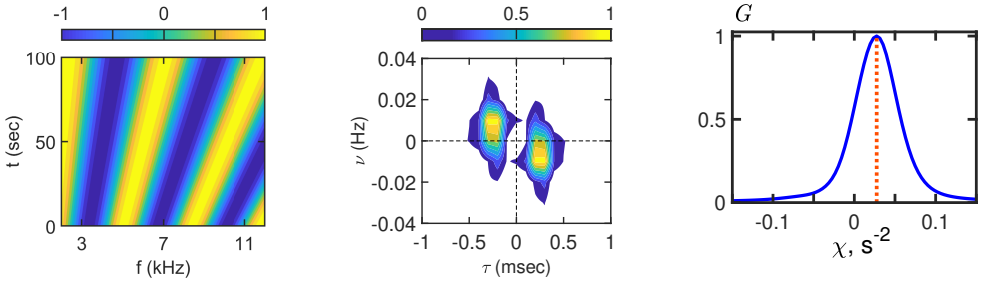

(a) (b) (c)

Figure 8. Interferogram $I_P(f,t)$ (a), hologram $F_P(\tau,\nu)$ (b), angular distribution $G_P(\chi)$ (c). Time: $\Delta t = 10.8 - 12.5$ min. Frequency: $\Delta f = 2.5 - 11.5$ kHz.

The structure of interferograms $I_X(f,t)$, $I_Y(f,t)$, $I_R(f,t)$, holograms $F_X(\tau,\nu)$, $F_Y(\tau,\nu)$, $F_R(\tau,\nu)$ and its angular distributions $G_X(\chi)$, $G_Y(\chi)$, $G_R(\chi)$ are the same as shown in Figures 6–8:

- The interferograms I_X, I_Y, I_R have the same slope of the interference fringes as I_P;
- the focal points are on the same straight line $\nu = \tilde{\varepsilon}\tau$ with the same angular coefficients in the hologram domain of F_X, F_Y, F_R as in the hologram domain of F_P;

- the angular distributions of the holograms G_X, G_Y, G_R have an extreme value at the same points.

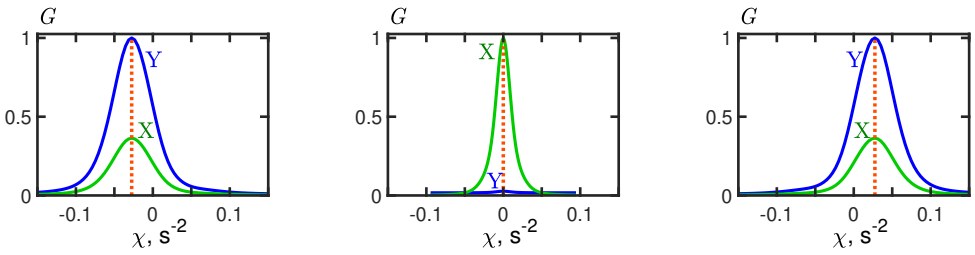

Figure 9. Angular distribution of holograms $G_X(\chi)$ (for V_X) and $G_Y(\chi)$ (for V_Y). Time: (a) $\Delta t = 2.5 - 4.2$ min; (b) $\Delta t = 6.7 - 8.4$ min; (c) $\Delta t = 10.8 - 12.5$ min. Frequency: $\Delta f = 2.5 - 11.5$ kHz.

The angular distributions of the holograms G_X, G_Y for three cases of source motion ($\Delta t = 2.5 - 4.2$ min; $\Delta t = 6.7 - 8.4$ min; $\Delta t = 10.8 - 12.5$ min) are shown in Figure 9. It can be seen that the shapes of G_X and G_Y, but the extreme values are different: - time interval $\Delta t = 2.5 - 4.2$ min: $G_Y(\chi_{\max})/G_X(\chi_{\max}) \approx -2.5$. This value of $|\tan\phi|$ corresponds to $\phi \approx -68$ degrees; - time interval $\Delta t = 6.7 - 8.4$ min: $G_Y(\chi_{\max})/G_X(\chi_{\max}) \approx 0$. This value of $|\tan\phi|$ corresponds to $\phi \approx 0$ degrees; - time interval $\Delta f = 2.5 - 11.5$ kHz: $G_Y(\chi_{\max})/G_X(\chi_{\max}) \approx +2.5$. This value of $|\tan\phi|$ corresponds to $\phi \approx +68$ degrees.

Using Eq. (20) $|\tan\phi| = G_Y(\chi_{\max})/G_X(\chi_{\max})$ and Eq. (21) the time dependence of the source bearing $\phi(t)$ can be calculated. The source bearing $\phi(t)$ reconstructed by numerical modeling for the time interval $\Delta t = 0 - 15$ min is shown in Figure 10. The blue solid line - source bearing corresponding to the trajectory geometry. The red dots - source bearings reconstructed by holographic signal processing. It can be seen that the source bearing values reconstructed within the numerical simulation are close to the true values.

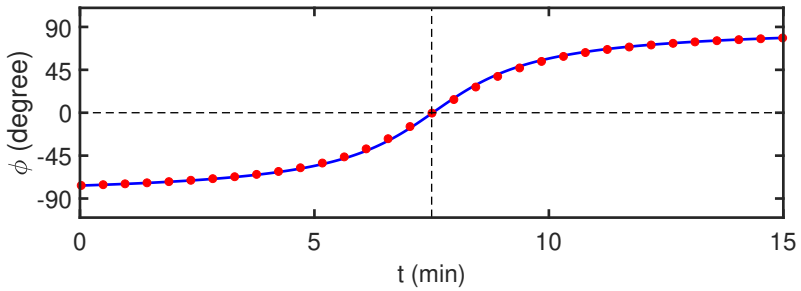

Figure 10. Time dependence of the source carrying $\phi(t)$. Time: $\Delta t = 0 - 15$ min. Frequency: $\Delta f = 2.5 - 11.5$ kHz. The blue solid line - source bearing according to the trajectory geometry. The red dots - source bearings reconstructed by holographic signal processing.

4. Experimental Results

Let us consider the experimental results of holographic signal processing in the high-frequency band in a natural shallow water waveguide. The depth of the water layer is $H = 8 - 10$ m. The distance from the coast $r \approx 2$ km. Three VSRs (VSR1, VSR2, VSR3) are placed at the vertices of the triangle at the bottom of the waveguide (Figure 11). A small, low-noise underwater source is used in the experiment for noise signal emission. The source velocity is $w = 1.5$ m/s. The source depth is $z_s = 4$ m. The noise source trajectory (A→B→C) in the horizontal plane of the experimental shallow water waveguide is shown in Figure 11.

The source trajectory parameters (Figure 11).

- motion time: $\Delta t = 0 - 18$ min;

- motion starting point: A;
- motion start time: $t = 14:13$;
- motion first track: along a straight line from point A to point B;
- motion first track time: $t = 14:13 - 14:24$;
- motion turning point: B;
- motion turning time: $t = 14:24$;
- motion second track: along a straight line from point B to point C;
- motion second track time: $t = 14:24 - 14:31$;
- motion finish point: C;
- motion finish time: $t = 14:31$;
- distance between point A and receiver VSR1 $\approx$ 990 m;
- distance between point A and receiver VSR2 $\approx$ 740 m;
- distance between point A and receiver VSR3 $\approx$ 810 m;
- distance between receiver VSR1 and receiver VSR2 $\approx$ 450 m;
- distance between receiver VSR1 and receiver VSR3 $\approx$ 440 m;
- distance between receiver VSR2 and receiver VSR3 $\approx$ 410 m;
- distance between receiver VSR1 and line connecting the receivers VSR2 and VSR3 $\approx$ 390 m.

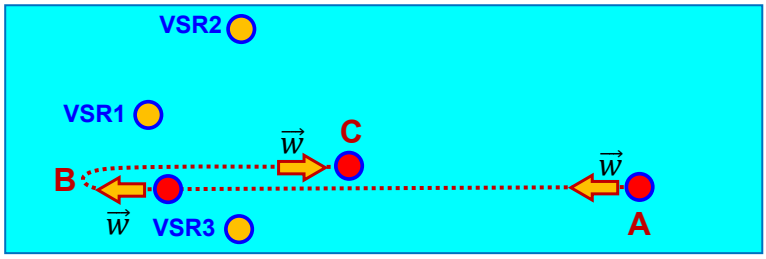

Figure 11. Experimental noise source trajectory. Horizontal plane. A - Starting point. B - turning point. C - finish point. VSR1, VSR2, VSR3 - positions at the vertices of the triangle at the waveguide bottom.

Let us consider experimental results of interferogram $I_P(f,t)$ for source moving along trajectory A→B→C (Figures 12–14) in time-frequency domain. The experimental results are obtained for frequency band $\Delta f = 0 - 2$ kHz and time interval $\Delta t = 14:10 - 14:35$. The motion of the first track A→B starts at 14:13. The motion of the first direct track A→B ends at 14:24. Point B is the turning point. Motion second reverse track B→C begins at 14:24. Motion second backward track B→C ends at 14:31. Duration of motion along the A→B→C trajectory $\Delta t = 17$ min.

During the experiment, the hydroacoustic signals of the moving noise source were recorded by four VSR channels: sound pressure P and three vibration velocity components V_X, V_Y, V_Z. The experimental interferogram $I_P(f,t)$ for receiver VSR1 is shown in the Figure 12. The experimental interferogram $I_P(f,t)$ for receiver VSR2 is shown in the Figure 13. The experimental interferogram $I_P(f,t)$ for receiver VSR3 is shown in the Figure 14. The change in the slope of the interference fringes indicates the movement of the source dynamics relative to the location of each VSR. In the case of the source moving from point A to the traverse point for each VSR, the slope of the interference fringes is negative $\delta f/\delta t < 0$, the period of the interferogram decreases T_f. It can be seen from the trajectory geometry (Figure 11) and experimental interferograms (Figures 12–14) that the traverse point time of the first motion track A→B is different for different VSR. The traverse point times are 14:21 (VSR1), 14:17:30 (VSR2), 14:17 (VSR3). The slope of the spurious fringes is zero approximately $\delta f/\delta t = 0$ for all VSR at the traverse points. When the noise source moves from the traverse point to the turning point B, the slope of the interference fringes is positive $\delta f/\delta t > 0$, the period of the interferogram increases T_f. The turning point B time is the same for each VSR - 14:24. In case the source moves from point B to traverse point for

each VSR, the fringes slope is negative $\delta f/\delta t < 0$, the interferogram period decreases T_f again.

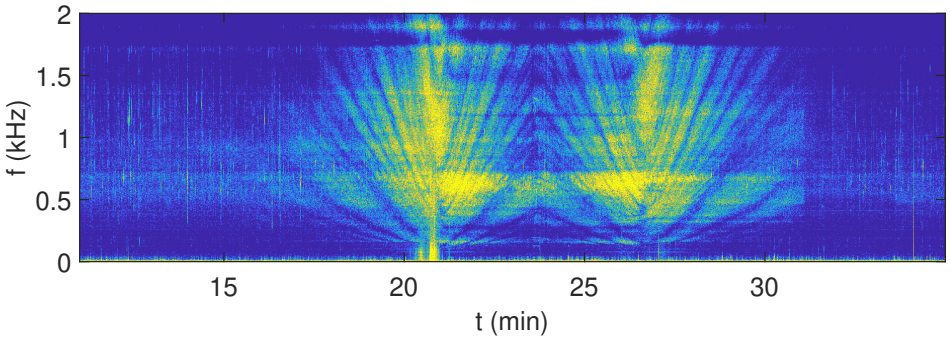

Figure 12. Experimental interferogram $I_P(f,t)$ of the sound pressure of a noise source moving along the trajectory A→B→C. Receiver: VSR1. Frequency $\Delta f = 0 - 2$ kHz. Time $\Delta t = 14:10 - 14:35$.

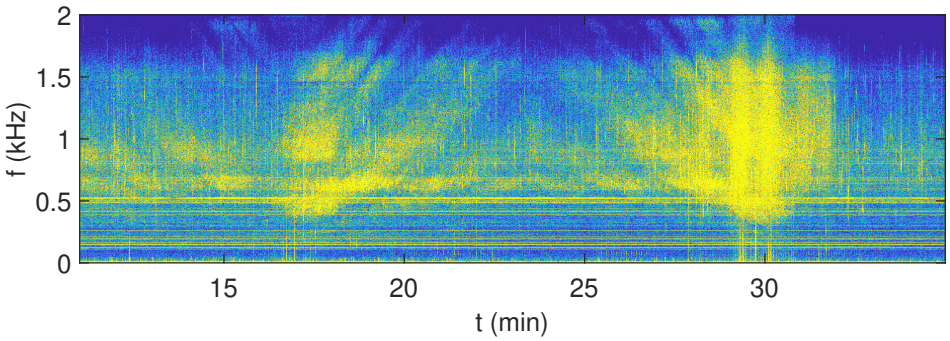

Figure 13. Experimental interferogram $I_P(f,t)$ of the sound pressure of a noise source moving along the trajectory A→B→C. Receiver: VSR2. Frequency $\Delta f = 0 - 2$ kHz. Time $\Delta t = 14:10 - 14:35$.

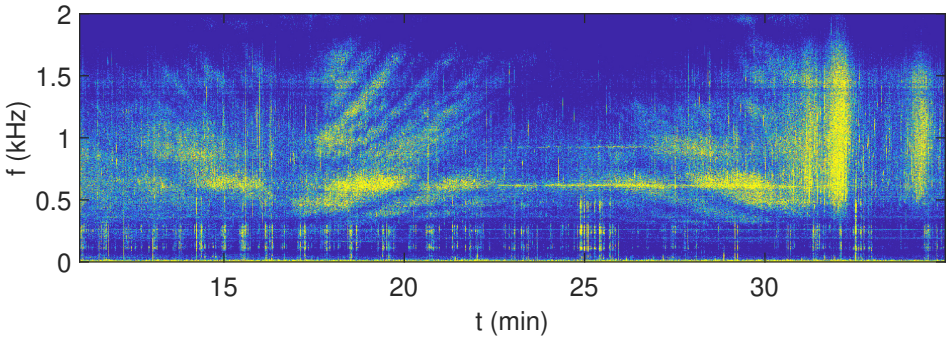

Figure 14. Experimental interferogram $I_P(f,t)$ of the sound pressure of a noise source moving along the trajectory A→B→C. Receiver: VSR3. Frequency $\Delta f = 0 - 2$ kHz. Time $\Delta t = 14:10 - 14:35$.

The traverse point time of the second track B→C is different for different VSRs. The traverse point times are 14:27 (VSR1), 14:30:00 (VSR2), 14:31:00 (VSR3). In the case of the source moving from traverse point C to for each VSR, the slope of the interference fringes is positive $\delta f/\delta t > 0$, the interferogram period increases T_f. When the noise source moves from the traverse point to the finish point C, the slope of the interference fringes is positive $\delta f/\delta t > 0$, the period of the interferogram increases T_f. The time of the end point C is the same for each VSR - 14:31.

The interferogram $I_P(f,t)$, the hologram $F_P(\tau,\nu)$ and the angular distribution $G_P(\chi)$ for different moments of the source motion are shown in Figures 15–19. The parameters of holographic signal processing are as follows. The frequency band from 0.7 kHz to 1.7 kHz,

$\Delta f = 1.0$ kHz. The $1Hz$ is a step in the frequency domain. The time interval is $\Delta t = 60$ sec with the parameters: $\delta t_1 = 1.5$ s, $\delta t_2 = 0.5$ s. The single interferogram consists of a spectrum of $J = 30$ temporary implementations.

The source was turned off at the beginning of the experiment. The interferogram $I_P(f,t)$, hologram $F_P(\tau,\nu)$ and angular distribution $G_P(\chi)$ corresponding to $t = 14:13$ and VSR1 are shown in Figure 15. It can be seen (Figure 15 (a)) that the interferogram $I_P(f,t)$ is a set of horizontal and vertical fringes. As a result, the hologram $F_P(\tau,\nu)$ (Figure 15 (b)) is a set of random focal spots. The angular distribution $G_P(\chi)$ has a set of peaks corresponding to other distant sources moving to and from VSR1.

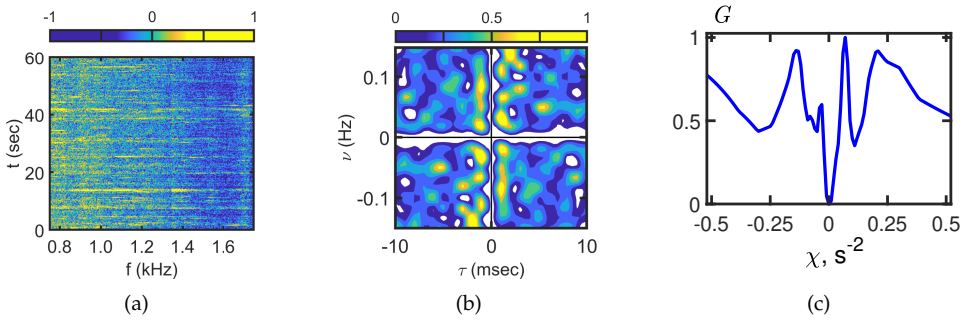

Figure 15. Interferogram $I_P(f,t)$ (a), hologram $F_P(\tau,\nu)$ (b), angular distribution $G_P(\chi)$ (c). Time: $t = 14:13$ min. Frequency: $\Delta f = 0.7 - 1.7$ kHz. Receiver: VSR1.

The interferogram $I_P(f,t)$, hologram $F_P(\tau,\nu)$ and angular distribution $G_P(\chi)$ corresponding to $t = 14:20$ and VSR1 are shown in Figure 16. The source moved from point A to the reverse point of VSR1 (Figure 11). It can be seen that the slope of the interference fringes is negative $\delta f/\delta t = -0.9 < 0$ kHz/min. As a result, the focal points are located at points on a straight line $\nu = \tilde{\varepsilon}\tau$ with an angular coefficient $\tilde{\varepsilon} = 20$ Hz/s in the hologram $F_P(\tau,\nu)$ domain (Figure 16 (b)). The angular distribution $G_P(\chi)$ has an extreme value at the point $\chi \approx 0.012\ s^{-2}$ (Figure 16 (c)).

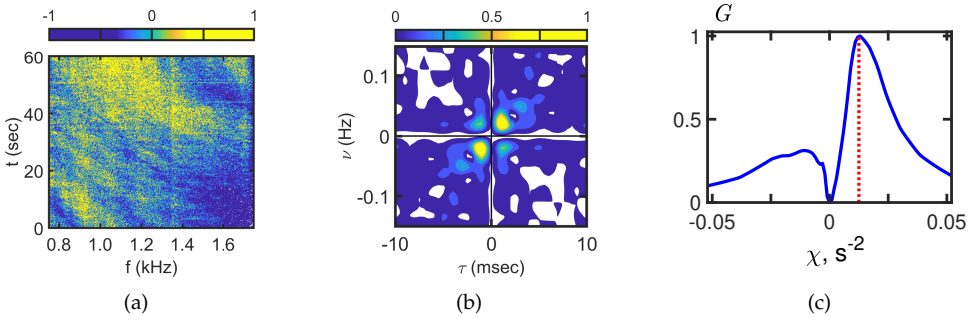

Figure 16. Interferogram $I_P(f,t)$ (a), hologram $F_P(\tau,\nu)$ (b), angular distribution $G_P(\chi)$ (c). Time: $t = 14:20$ min. Frequency: $\Delta f = 0.7 - 1.7$ kHz. Receiver: VSR1.

At $t = 14:23$ the source moved from A→B from the traverse point for VSR1 to point B (Figure 11). The interferogram $I_P(f,t)$, hologram $F_P(\tau,\nu)$ and angular distribution $G_P(\chi)$ corresponding to $t = 14:23$ and VSR1 are shown in Figure 17. It can be seen that the slope of the interference fringes is positive $\delta f/\delta t = 0.5 > 0$ kHz/min. There are two groups of focal points on different straight lines $\nu = \tilde{\varepsilon}\tau$ in the hologram $F_P(\tau,\nu)$ domain (Figure 17 (b)). One of them corresponds to $\tilde{\varepsilon} = -10$ Hz/s. The other corresponds to $\tilde{\varepsilon} = -5$ Hz/s. The angular distribution $G_P(\chi)$ has a main extreme at the point $\chi \approx -0.007\ s^{-2}$ (Figure 17 (c)).

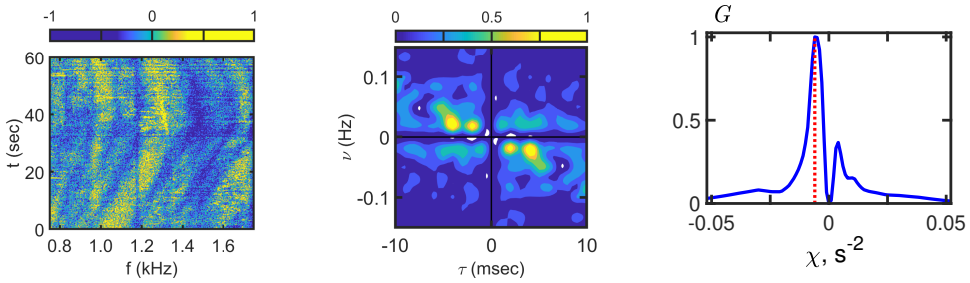

(a) (b) (c)

Figure 17. Interferogram $I_P(f,t)$ (a), hologram $F_P(\tau,\nu)$ (b), angular distribution $G_P(\chi)$ (c). Time: $t = 14:23$ min. Frequency: $\Delta f = 0.7 - 1.7$ kHz. Receiver: VSR1.

At the end of the experiment ($t = 14:30$), the source moved from the traverse point for VSR1 to point C (Figure 11). The interferogram $I_P(f,t)$, hologram $F_P(\tau,\nu)$ and angular distribution $G_P(\chi)$ corresponding to $t = 14:30$ and VSR1 are shown in Figure 18. It can be seen that the slope of the interference fringes is positive $\delta f/\delta t = 0.4 > 0$ kHz/min. There are two groups of focal points on different straight lines $\nu = \tilde{\varepsilon}\tau$ in the hologram $F_P(\tau,\nu)$ domain (Figure 18 (b)). One of them corresponds to $\tilde{\varepsilon} = -11$ Hz/s. The other corresponds to $\tilde{\varepsilon} = -6$ Hz/s. The angular distribution $G_P(\chi)$ has a major extreme at the point $\chi \approx -0.006\ s^{-2}$ (Figure 18 (c)).

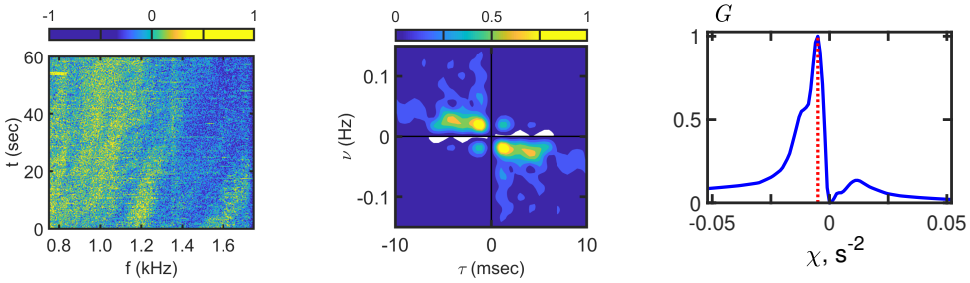

(a) (b) (c)

Figure 18. Interferogram $I_P(f,t)$ (a), hologram $F_P(\tau,\nu)$ (b), angular distribution $G_P(\chi)$ (c). Time: $t = 14:30$ min. Frequency: $\Delta f = 0.7 - 1.7$ kHz. Receiver: VSR1.

The results of holographic signal processing noise filtering are shown in Figure 19 for VSR1, time $t = 14:19$ min, frequency band $\Delta f = 0.7 - 1.7$ kHz. The interferogram $I_P(f,t)$, hologram $F_P(\tau,\nu)$ and angular distribution $G_P(\chi)$ corresponding to $t = 14:30$ for the experimental data are shown in Figure 19 (a), (b), (c). The results of noise filtering are shown in Figure 19 (d), (e), (f). It can be seen that the interference fringes of the experimental interferogram $I_P(f,t)$ are blurred (Figure 19 (a)). The focal points of the hologram $F_P(\tau,\nu)$ are in the background noise (Figure 19 (b)). The filtering of the spectral density of the hologram $F_P(\tau,\nu)$ is carried out in the band represented by the dotted line (Figure 19 (e)). It can be seen that the extreme values at the point are the same for the experimental angular distribution $G_P(\chi)$ (Figure 19 (c)) and for the angular distribution $G_P(\chi)$ after noise filtering (Figure 19 (f)). The filtered interferogram $I_P(f,t)$ is in (Figure 19 (d)). It can be seen that the filtered interferogram has more contrast. The interference fringes have the same slope angle.

Using Eq. (20) $|\tan\phi| = G_Y(\chi_{\max})/G_X(\chi_{\max})$ and Eq. (21) the time dependence of the source bearing $\phi(t)$ can be calculated. The source bearing $\phi(t)$ reconstructed by holographic signal processing of experimental data for time interval $\Delta t = 14:10 - 14:35$ min and frequency band $\Delta f = 0.7 - 1.7$ kHz is shown in Figures 20–22. The Figure 20 corresponds to VSR1. The Figure 21 corresponds to VSR2. The Figure 22 corresponds to VSR3. The blue solid line - source bearing corresponding to the trajectory geometry. The red dots - source

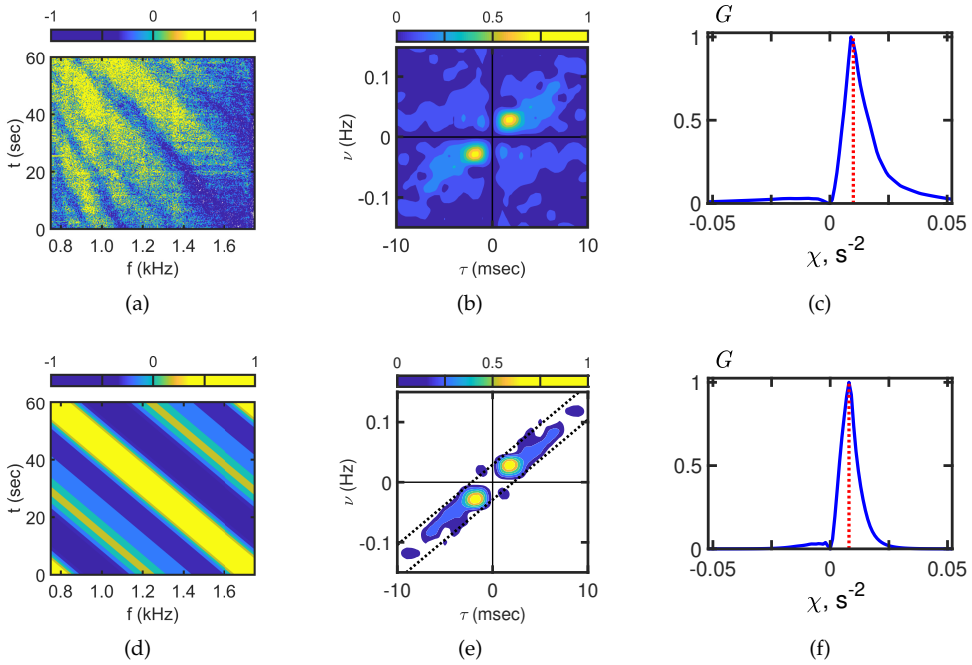

Figure 19. Results of the noise filtering in holographic signal processing. (a) Interferogram $I_P(f,t)$ - experiment. (b) Hologram $F_P(\tau,\nu)$ - experiment. (c) Angular distribution $G_P(\chi)$ - experiment. (d) Interferogram $I_P(f,t)$ - noise filtering result. (e) Hologram $F_P(\tau,\nu)$ - noise filtering result. (f) Angular distribution $G_P(\chi)$ - noise filtering result. Time: $t = 14:19$ min. Frequency: $\Delta f = 0.7 - 1.7$ kHz. Receiver: VSR1.

bearings reconstructed by holographic signal processing. It can be seen that the source bearings reconstructed by holographic signal processing are close to the experimental values.

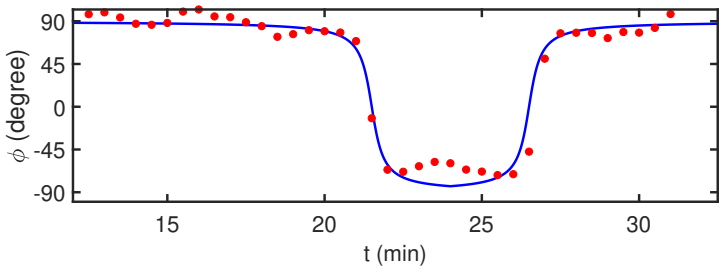

Figure 20. Temporal dependence of the source bearing $\phi(t)$. Receiver: VSR1. Time: $\Delta t = 14:10 - 14:35$ min. Frequency: $\Delta f = 0.7 - 1.7$ kHz. The blue solid line - source bearing according to the trajectory geometry. The red dots - source bearings reconstructed by holographic signal processing of the experimental data.

5. Conclusions

The method of formation of 2D interferogram and 2D hologram of a noise source by a vector scalar receiver in the high-frequency band ($\approx 0 - 10$ kHz) in a shallow water waveguide (≈ 10 m) is presented in the paper. The interferograms $I_P(f,t)$, $I_X(f,t)$, $I_Y(f,t)$ and the holograms $F_P(\tau,\nu)$, $F_X(\tau,\nu)$, $F_Y(\tau,\nu)$ for different channels of the VSR: P - sound pressure; V_X, V_Y - horizontal components of vibrational velocities are considered for different frequency bands.

It is shown that the 2D interferogram consists of parallel interference fingers in the presence of a moving noise source. As a result, the hologram contains focal points located

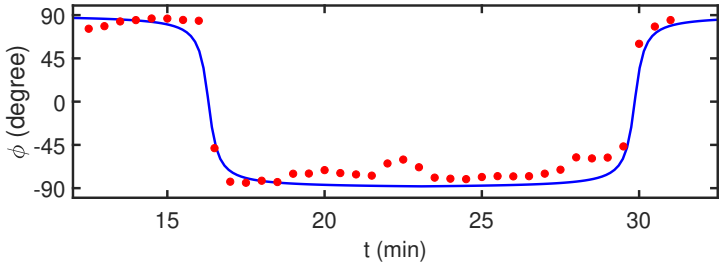

Figure 21. Temporal dependence of the source bearing $\phi(t)$. Receiver: VSR2. Time: $\Delta t = 14:10-14:35$ min. Frequency: $\Delta f = 0.7-1.7$ kHz. The blue solid line - source bearing according to the trajectory geometry. The red dots - source bearings reconstructed by holographic signal processing of the experimental data.

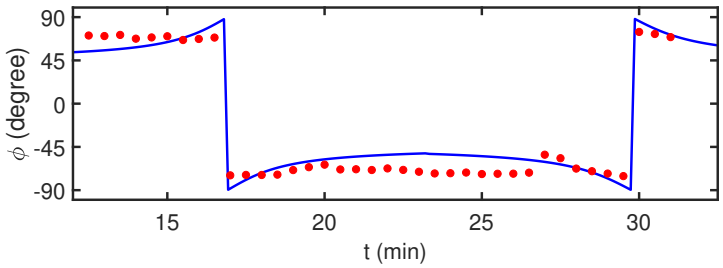

Figure 22. Temporal dependence of the source bearing $\phi(t)$. Receiver: VSR3. Time: $\Delta t = 14:10-14:35$ min. Frequency: $\Delta f = 0.7-1.7$ kHz. The blue solid line - source bearing according to the trajectory geometry. The red dots - source bearings reconstructed by holographic signal processing of the experimental data.

on a straight line $\nu = \tilde{\varepsilon}\tau$ with an angular coefficient $\tilde{\varepsilon}$. In presence of moving source the angular distribution of holograms $G_P(\chi)$, $G_X(\chi)$, $G_Y(\chi)$ has the main extreme value at $\chi_{\max}$. Thus, it is possible to detect and locate the noise source in the shallow water waveguide within the framework of holographic signal processing by using this feature of the hologram and its angular distribution.

The moving direction of the noise source can be estimated from the slope of the interference fringes and the angular coefficient of the straight line $\nu = \tilde{\varepsilon}\tau$ of the focal points in the hologram. When the noise source moves to the VSR, the slope of the interference fringes has a negative value $\delta f/\delta t < 0$. The hologram focal points are in the first and third quadrants of the hologram domain $\tilde{\varepsilon} > 0$. The coordinate of the main extreme value ($\chi_{\max} > 0$) of the angular distribution $G_P(\chi)$ is in the positive range. When the noise source moves away from the VSR, the slope of the interference fringes has positive value $\delta f/\delta t > 0$. The hologram focal points are located in the second and fourth quadrants of the hologram domain $\tilde{\varepsilon} < 0$. The coordinate of the main extreme value ($\chi_{\max} < 0$) of the angular distribution $G_P(\chi)$ is in the negative range. When the noise source moves in the traverse point of the VSR, the interference fringes are parallel to the frequency f-axis in the interferogram domain. The hologram focal points are located on the time τ-axis in the hologram domain: $\tilde{\varepsilon} = 0$. The coordinate of the main extreme value ($\chi_{\max} = 0$) of the angular distribution $G_P(\chi)$ is located at the origin of the axis.

The results of noise filtering within the framework of holographic signal processing are presented in the paper. It is shown that the interference fringes of the experimental interferogram are blurred. The focal points of the hologram lie in the background noise. The extreme values $\chi_{\max}$ are at the same points for the experimental $G_P^e(\chi)$ and for $G_P^f(\chi)$ after noise filtering. The filtered interferogram $I_P(f,t)$ becomes more contrasted. The interference fringes have the same slope angle.

It is shown in the paper that within the framework of holographic signal processing the temporal dependence of the source bearing $\phi(t)$ is estimated using the relation between

$G_X(\chi_{\max})$ and $G_Y(\chi_{\max})$. The results of the source bearing reconstruction within the framework of numerical simulation and experimental data processing. The values of the source bearings reconstructed within the framework of holographic signal processing are close to the values defined by the geometry of the source trajectory.

Author Contributions: Supervision and project administration, M.E.; conceptualization and methodology, V.K. and S.P.; experiment Y.M.; software, S.T., P.R.; validation, S.P., V.K. and Y.M.; formal analysis, M.E. and S.P.; writing – original draft preparation, M.E. and S.P.; writing – review and editing, M.E. and S.P.; All authors have read and agreed to the published version of the manuscript.

Funding: This work was supported by grant from the Russian Science Foundation № 23-61-10024, https://rscf.ru/project/23-61-10024/

Data Availability Statement: The data presented in this study are available on request from the corresponding author.

Conflicts of Interest: The authors declare no conflict of interest.

References

1. Baggeroer, A.B.; Kuperman, W.A.; Schmidt, H. Matched field processing: Source localization in correlated noise as an optimum parameter estimation problem. *J. Acoust. Soc. Am., 83(2):571–587.* **1998**.
2. Jackson, D.R.; Ewart, T.E. The effect of internal waves on matched-field processing. *J. Acoust. Soc. Am., 96(5):2945–2955.* **1994**.
3. Dosso, S.E.; Nielsen, P.L.; Wilmut, M.J. Data error covariance in matched-field geoacoustic inversion. *J. Acoust. Soc. Am., 119:208–219.* **2006**.
4. Sazontov, A.G.; Malekhanov, A.I. Matched field signal processing in underwater sound channels. *Acoust. Phys., 61:213–230.* **2015**.
5. Chuprov S. Interference structure of a sound field in a layered ocean. *Ocean Acoust., Curr. State., 71–91.* **1982**.
6. Weston D.; Stevens K. Interference of wide-band sound in shallow water. *J. Sound Vibr., 21(1):57–64.* **1972**.
7. Grachev, G.; Wood, J. Theory of acoustic field invariants in layered waveguides. *Acoust. Phys. 39 (1):33–35.* **1993**.
8. Orlov, E.F.; Sharonov, G.A. Interference of Sound Waves in the Ocean. *Dal'nauka,* **1998**.
9. Ianniello, J. Recent developments in sonar signal processing. *IEEE Signal Proc. Magazine, 15(4):27-40.* **1998**.
10. Kuperman, W.A.; D'Spain, G.L. Ocean acoustic interference phenomena and signal processing. *Ocean Acoust. Interfer. Phenom. Signal Proc. 621* **2002**.
11. D'Spain, G.L.; Kuperman, W.A. Application of waveguide invariants to analysis of spectrograms from shallow water environments that vary in range and azimuth. *J. Acoust. Soc. Am., 106:2454–2468* **1999**.
12. Heaney, K.; Cox, H. Rapid geoacoustic characterization for limiting environmental uncertainty for sonar system performance prediction," in Impact of Littoral Environmental Variability on Acoustic Predictions and Sonar Performance. *Pace, N.; Jensen, F.B. (eds.) Kluwer Academic, Dordrecht, 123–130* **2002**.
13. Thode, A.M. Source ranging with minimal environmental information using a virtual receiver and waveguide invariant theory. *J. Acoust. Soc. Am., 108:1582–1594* **2000**.
14. Hodgkiss, W.; Song, H.; Kuperman, W.; Akal, T.; Ferla, C.; Jackson, D. A long-range and variable focus phase-conjugation experiment in a shallow water. *J. Acoust. Soc. Am., 105:1597–1604* **1999**.
15. Thode, A.M.; Kuperman, W.A.; D'Spain, G.L.; Hodgkiss, W.S. Localization using Bartlett matched-field processor sidelobes. *J. Acoust. Soc. Am., 107:278–286* **2000**.
16. Yang, T.C. Motion compensation for adaptive horizontal line array processing. *J. Acoust. Soc. Am., 113:245–260* **2003**.
17. Yang, T.C. Beam intensity striations and applications. *J. Acoust. Soc. Am., 113:1342–1352* **2003**.
18. Rouseff D.; Leigh, C.V. Using the waveguide invariant to analyze Lofargrams. *In Proceedings of the Oceans '02 MTS/IEEE 4:2239–2243.* **2002**.
19. Thode, A.M. Source ranging with minimal environmental information using a virtual receiver and waveguide invariant theory. *J. Acoust. Soc. Am., 108(4):1582-1594.* **2000**.
20. Rouseff, D.; Spindel, R.C. Modeling the waveguide invariant as a distribution. *AIP Conf. Proc., Amer. Inst. Phys., 621:137-150.* **2002**.
21. Baggeroer, A.B. Estimation of the distribution of the interference invariant with seismic streamers. *AIP Conf. Proc., Amer. Inst. Phys., 621:151-170.* **2002**.
22. Heaney, K.D. Rapid geoacoustic characterization using a surface ship of opportunity. *IEEE J. Oceanic Engrg., 29(1):88-99.* **2004**.
23. Cockrell, K.L.; Schmidt, H. Robust passive range estimation using the waveguide invariant. *J. Acoust. Soc. Am., 127(5):2780-2789.* **2010**.
24. Rouseff D.; Zurk, L.M. Striation-based beam forming for estimating the waveguide invariant with passive sonar. *J. Acoust. Soc. Am. Express Lett., 130:76–81.* **2011**.
25. Harrison, C.H. The relation between the waveguide invariant, multipath impulse response, and ray cycles. *J. Acoust. Soc. Am., 129(5):2863-2877.* **2011**.

26. Emmetiere. R.; Bonnel, J.; Gehant, M.; Cristol, X.; Chonavel, Th. Understanding deep-water striation patterns and predicting the waveguide invariant as a distribution depending on range and depth. *J. Acoust. Soc. Am., 143(6):3444-3454.* **2018**.
27. Emmetiere. R.; Bonnel, J.; Cristol, X.; Gehant, M.; Chonavel, Th. Passive source depth discrimination in deep-water. *IEEE J. Select. Topics Signal Process., 13(1):185-197.* **2019**.
28. Wang, N. Dispersionless transform and potential application in ocean acoustics. *In Proceedings of the 10th Western Pacific Acoustics Conference, Beijing, China.* **2009**.
29. Gao, D.; Wang, N. Dispersionless transform and signal enhancement application. *In Proceedings of the 2th International Conference on ShallowWater Acoustic, Shanghai, China.* **2009**.
30. Gao, D.; Wang, N. Dispersionless transform and signal enhancement application. *In Proceedings of the 3th Oceanic Acoustics Conference, Beijing, China.* **2012**.
31. Xiao-Le, G.; Kun-De, Y.; Yuan-Liang, M.; Qiu-Long, Y. A source range and depth estimation method based on modal dedispersion transform. *Acta Phys. Sin., 65:214302.* **2016**.
32. Zhang, S.; Zhang, Y.; Gao, S. Passive acoustic location with de-dispersive transform. *In Proceedings of the 16th Western China Acoustics Conference, Leshan, Sichuan, China.* **2016**.
33. Lee, S.; Makris, N.C. A new invariant method for instantaneous source range estimation in an ocean waveguide from passive beam-time intensity data. *J. Acoust. Soc. Am., 116:2646.* **2004**.
34. Lee, S.; Makris, N.C. The array invariant. *J. Acoust. Soc. Am., 119:336–351.* **2006**.
35. Lee, S. Efficient Localization in a Dispersive Waveguide: Applications in Terrestrial Continental Shelves and on Europa. *Ph.D. Thesis, Massachusetts Institute of Technology, Cambridge, MA, USA.* **2006**.
36. Kuz'kin, V.M.; Pereselkov, S.A.; Kuznetsov, G.N. Spectrogram and localization of a sound source in a shallow sea. *Acoust. Phys. 63(4):449-461* **2017**.
37. Pereselkov, S.A.; Kuz'kin, V.M. Interferometric processing of hydroacoustic signals for the purpose of source localization *J. Acoust. Soc. Am. 151(2):666-676* **2022**.
38. Ehrhardt, M.; Pereselkov, S.A.; Kuz'kin, V.M.; Kaznacheev, I.; Rybyanets, P. Experimental observation and theoretical analysis of the low-frequency source interferogram and hologram in shallow water. *J. Sound Vibr., 544:117388.* **2023**.
39. Kuz'kin, V.M.; Pereselkov, S.A.; Kuznetsov, G.N.; Grigor'ev, V.A. Resolving power of the Interferometric method of source localization. *Phys. Wave Phenom. 26(2):150-159* **2018**.
40. Kuz'kin, V.M.; Pereselkov, S.A.; Matvienko, Yu.V.; Lyakhov, G.A.; Tkachenko, S.A. Noise source detection in an oceanic waveguide using interferometric processing. *Phys. Wave Phenom. 28(1):68-74* **2020**.
41. Kuz'kin, VM; Pereselkov, S.A.; Zvyagin, V.G.; Malykhin A.Yu.; Prosovetskiy, D.Yu. Intense internal waves and their manifestation in interference patters of received signals on oceanic shelf. *Phys. Wave Phenom. 26(2):160-167.* **2018**.
42. Pereselkov, S.; Kuz'kin, V.; Ehrhardt, M.; Tkachenko, S.; Rybyanets, P.; Ladykin, N. Three-Dimensional Modeling of Sound Field Holograms of a Moving Source in the Presence of Internal Waves Causing Horizontal Refraction *J. Mar. Sci. Eng. 11(10):1922* **2023**.
43. Gordienko, V.A. Vector-Phase Methods in Acoustics *Moscow : FIZMATLIT, 480 [in Russian]* **2007**.
44. Nehorai, A.; Paldi, E. Acoustic vector sensor array processing. *J. Acoust. Soc. Am. 51:1479–1491* **1994**.
45. Cao, J.; Liu, J.; Wang, J.; Lai, X. Acoustic vector sensor: Reviews and future perspectives *IET Signal Process. 11:1–9* **2017**.
46. Shi, J.; Dosso, S.E.; Sun, D.; Liu, Q. Geoacoustic inversion of the acoustic-pressure vertical phase gradient from a single vector sensor. *J. Acoust. Soc. Am. 146:3159–3173* **2019**.
47. Wang, W.; Li, X.; Zhang, K.; Shi, J.; Shi, W.; Ali, W. Robust Direction Finding via Acoustic Vector Sensor Array with Axial Deviation under Non-Uniform Noise. *J. Mar. Sci. Eng. 10:1196* **2022**.
48. Jensen, F.B.; Kuperman, W.A.; Porter, M.B.; Schmidt, H.; Tolstoy, A. Computational Ocean Acoustics. *Springer.* **2011**.
49. Brekhovskikh, L.M.; Lysanov, Y.P. Fundamentals of Ocean Acoustics. *Springer.* **2013**.